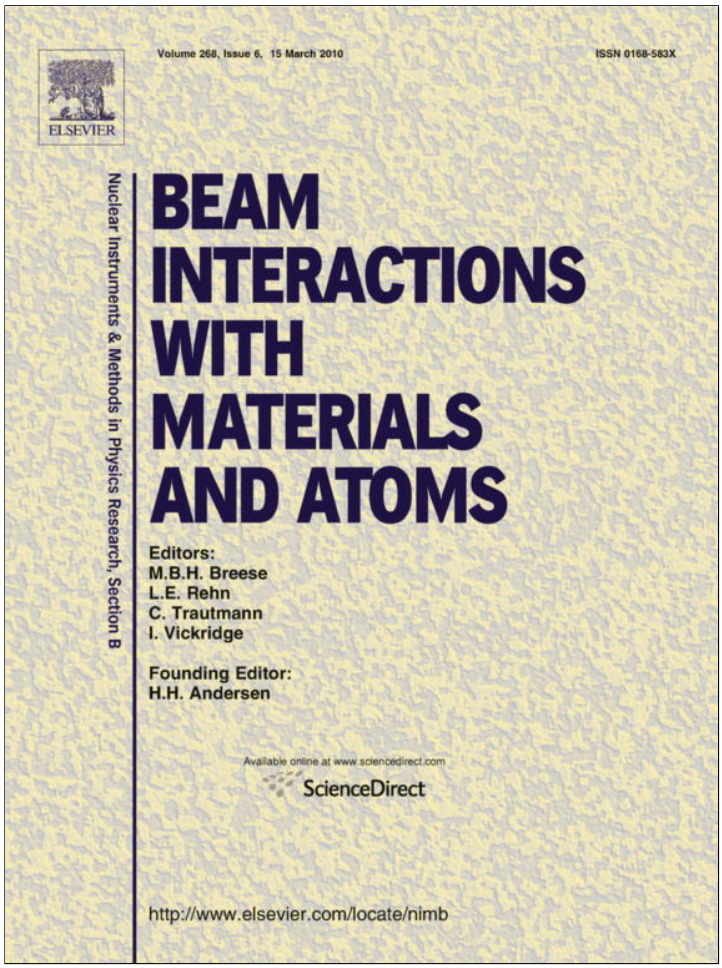

Nuclear Instruments and Methods in Physics Research B 268 (2010) 657–670

Contents lists available at ScienceDirect

Nuclear Instruments and Methods in Physics Research B

journal homepage: www.elsevier.com/locate/nimb

A study of on-line gas cell processes at IGISOL

I.D. Moore [a,*], T. Kessler [a], T. Sonoda [a,1], Y. Kudryavstev [b], K. Peräjärvi [a,c], A. Popov [d], K.D.A. Wendt [e], J. Äystö [a]

[a] Department of Physics, University of Jyväskylä, P.O. Box 35 (YFL), FI-40014 Jyväskylä, Finland
[b] Instituut voor Kern-en Stralingsfysika, University of Leuven, Celestijnenlaan 200 D, B-3001 Leuven, Belgium
[c] STUK-Radiation and Nuclear Safety Authority, P.O. Box 14, FI-00881 Helsinki, Finland
[d] Petersburg Nuclear Physics Institute, Gatchina, St-Petersburg 188350, Russia
[e] Institut für Physik, Johannes Gutenberg-Universität, 55099 Mainz, Germany

ARTICLE INFO

Article history:
Received 27 January 2009
Received in revised form 21 November 2009
Available online 11 December 2009

Keywords:
Gas cell
Laser resonance ionization
Ion-electron recombination
Molecular formation
Ion guide

ABSTRACT

The laser ion source at the IGISOL facility, Jyväskylä, has been used to study the effects of the passage of a primary beam through an ion guide via the dynamic time profiles of yttrium and related molecular compounds. The accessibility of a neutral fraction for laser ionization is shown to be restricted to the nozzle region in the presence of a weak plasma. The survival of this neutral fraction cannot be explained by recombination of the buffer gas alone and perhaps indicates a suppression of the transport of ions due to a plasma-generated electric field. The concept of a competition between the processes that create and destroy the ion of interest is used to explain the different trends in the ratio of yttrium to yttrium oxide following the extraction of a stopped primary beam of $^{89}Y^{21+}$ in both helium and argon buffer gases.

1. Introduction

In our previous article we presented the first detailed off-line studies using the new laser ion source at the IGISOL facility, Jyväskylä [1]. The flexibility of the dye-Ti:Sapphire laser system was illustrated using the laser ionization of yttrium atoms produced in an ion guide via the resistive heating of a filament. A careful study was undertaken to understand the effects of gas purity on an element that exhibits strong molecular formation in the presence of impurities within the gas. In order to decouple the competition between the molecular formation process and evacuation from the ion guide we analyzed the experimental data in the framework of a series of molecular rate equations in order to extract time profiles of single laser shots. With good control over the gas purification a sub-ppb level of impurities was demonstrated. The importance of the baseline vacuum pressure in the immediate vicinity of the ion guide was apparent after a controlled leak was added to the IGISOL chamber. Within the experimentally determined flight time of ~100 μs through the rf sextupole ion beam guide (SPIG) [2], a fast redistribution of atomic ions into molecular forms can occur after leaving the exit nozzle of the gas cell highlighting the importance of having a clean environment not only within the gas cell but through which the ions are electrostatically guided following extraction.

In this follow-up paper the results of our first set of on-line experiments undertaken in conditions of high ion-electron density are presented. On-line experiments pose an additional set of challenges to attaining that of sub-ppb purity conditions. One of the most important loss mechanisms for the ion of interest on-line is that of neutralization. This is due to the density of ionization created either by the passage of a primary beam or via the extraction of recoils out from the gas cell from a fixed target such as in a light-ion induced fusion-evaporation reaction or that of a fission reaction. The effects associated with the presence of a large density of ion-electron pairs have been discussed previously [3,4]. The resultant reduction in extraction efficiency as a function of the implantation rate has been observed at all gas catcher facilities [5–8] which incorporate different volumes, buffer gases, projectile energies and electric fields. A review of the most recent results highlighting the decline in extraction efficiency and possible solutions to tolerate higher primary beam intensities can be found in [9].

The experiments discussed in the present work continue the studies utilizing the yttrium atomic system. As an intermediate step towards an operational ion guide laser ion source facility it is important to understand the competing processes occurring in the gas cell under on-line conditions. The effects of the passage of a primary beam through the ion guide have been studied using the time distribution profiles of yttrium and associated molecules.

* Corresponding author. Tel.: +358 14 2602430; fax: +358 14 2602351.
E-mail address: iain.d.moore@jyu.fi (I.D. Moore).
[1] Present address: Nishina Center for Accelerator Based Science, RIKEN, 2-1 Hirosawa, Wako, Saitama 351-0198, Japan.

0168-583X/$ - see front matter © 2009 Elsevier B.V. All rights reserved.
doi:10.1016/j.nimb.2009.12.001

Information has been extracted from both the equilibrated processes and the dynamic effects, with the latter discussed using two different models. Additionally, a stopped primary beam of yttrium has been extracted from the ion guide and the ratio of yttrium to yttrium oxide as a function of gas pressure has been studied in both helium and argon. The ratio has been explained using a simple model of creative and destructive processes within the gas cell. Although our goal is not to produce detailed simulations of the ion guide processes, in order to provide a more efficient and selective means of producing low-energy radioactive ion beams via laser ionization, a reasonable understanding of the ion guide plasma is required. Finally, we note that in those instances in which laser ionization has been used in the current studies, the laser ionization efficiency is not a subject of discussion. The choice of laser ionization scheme included a non-saturated intermediate excitation step and a non-resonant ionization step. Without the use of Rydberg- or auto-ionization states the cross section for ionization is reduced by a factor of ~1000. Future radioactive ion beam production with the laser ion source will utilize the most efficient ionization scheme.

2. Experimental set-up

The laser system used in this work has been described in detail in our previous article [1] therefore we concentrate here on the IGISOL front-end. It is informative to briefly mention the present ion guides in regular use at IGISOL, in order to explain the differences between these and the gas cells designed for the purpose of laser ionization studies. There are three main types of ion guide: light-ion ion guide, heavy-ion ion guide and a fission ion guide. The differences between each relate to the choice of reaction kinematics needed for a particular experiment. In addition, two other ion guides have been developed for specific purposes. The first has been designed for quasi- and deep-inelastic reactions [10], and the second for the production of a low-energy ion beam of daughter products of α-emitters [11].

The light-ion ion guide has been designed for use with H and He primary beams. In this guide the target is mounted directly in the stopping volume of the cell as the recoil energy of the reaction products is small. The effective stopping volume for the recoils is ~3 cm^3 and with a typical exit nozzle diameter of 1.2 mm, the extraction time can be as short as one millisecond. A typical ion guide efficiency (ions detected in the separator focal plane compared to those recoiling out of the target into the stopping volume) varies between 1% and 10% [12].

The heavy-ion ion guide (HIGISOL) is used in heavy-ion induced fusion-evaporation reactions. As the reaction product distribution is forward peaked a special arrangement is needed to reduce the strong ionization of the helium gas by the accelerator beam. The so-called "shadow method" is employed which takes advantage of the difference between the primary beam angular distribution and that of the reaction products after passing through a relatively thick target (few mg/cm^2) [13–15]. The stopping volume is considerably larger than that of the light-ion ion guide, typically 120 cm^3. With a similar size exit nozzle an average evacuation time of 185 ms can be estimated by dividing the stopping chamber volume with the exit-hole conductance. Targets are installed on a water cooled frame outside the stopping volume, with a variable distance relative to the ion guide along the cyclotron beam axis. Recently, a rotating target wheel was installed and used in combination with the HIGISOL system. Ion guide efficiencies are rather low, on the order of 1×10^{-3}.

Many of the experimental studies at IGISOL use the fission ion guide. The guide has been designed for use in proton-induced fission of uranium (or other actinide) targets. A 15 mg/cm^2 uranium target is mounted within the ion guide volume at an angle of 7° with respect to the primary beam to increase the effective thickness of the target to 123 mg/cm^2. In order to reduce the beam-related plasma, the primary beam is shielded from the stopping chamber with a thin foil. The volume of this chamber, 130 cm^3, is comparable to that of the HIGISOL ion guide. The separation foil may be made of an element of choice to provide sputtered material for use as a stable ion beam for on-line experimental calibrations.[2] Although the fission fragments can be separated from the primary beam due to the isotropic emergence from the target, an intense plasma effect remains, generated by the fission fragments themselves passing through the stopping gas. Combining the recombination losses with a relatively low fission fragment stopping efficiency of ~1% in 200 mbar helium, typical absolute efficiencies are rather low, only a few $\times 10^{-4}$, and very often the isotope of interest is dominated by less exotic, unwanted isobars. It should be noted, that the fission rate in the target is $\sim 2 \times 10^9$ fissions/μC. Despite this, maximum intensities of ~10^5 fission products per second can be achieved with the ion guide technique.

Two laser ion guides have been used in studies of laser ionization at the IGISOL facility. The first, used in the present work and on loan from the LISOL group at the University of Leuven, has been described in detail in [1]. Briefly, the volume of the gas cell can be divided into two parts, the main cell and a channel of 10 mm in diameter and 26 mm in length leading to the exit nozzle. The conductance of the 0.5 mm diameter exit hole for helium is equal to 0.112 l/s. The evacuation time of the whole guide is ~480 ms and that of the exit channel ~18 ms. Compared to the ion guides described above these extraction times are considerably longer due to the smaller exit hole. This is necessary in order to achieve neutralization of the recoiling nuclei. The second ion guide is a modified version of the HIGISOL gas cell, built for both the laser ion source project in Jyväskylä and standard heavy-ion fusion-evaporation reactions. The guide has been optimized for efficient gas flow transport, water cooling and baking capabilities have been added and the design is modular such that filaments and dc electrodes can be installed. The ion guide has three main components: a gas feeding part, the main body and a removable exit nozzle, all of which are sealed with indium. A beam window of 48 mm in diameter can be added for standard HIGISOL reactions. A schematic picture of both the LISOL ion guide and the JYFL laser ion guide is shown in Fig. 1. The volume of the main body of the JYFL ion guide up to the exit nozzle is ~252 cm^3, almost a factor of five larger than the LISOL guide. The evacuation time of the ion guide volume for an exit hole of 0.5 mm diameter is 2.25 s, and for a standard exit nozzle diameter of 1.2 mm, 390 ms.

3. Processes within the gas cell under on-line conditions

On-line experiments provide an additional set of complex processes to those of the off-line conditions discussed in our earlier work [1]. In this section we present an overview of processes occurring within the ion guide, often in parallel, relevant to the experimental results presented in later sections.

The monomer buffer gas ions B^+ created by the passage of a primary accelerator beam through an ion guide, or in the passage of energetic highly-charged fragment recoils, rapidly dimerize to B_2^+ in the three-body reaction:

$$B^+ + 2B \rightarrow B_2^+ + B. \quad (1)$$

[2] In collinear laser spectroscopy of neutron-rich fission fragments a stable calibration is often required to connect the change in mean-square charge radii of radioactive isotopes to stable isotopes.

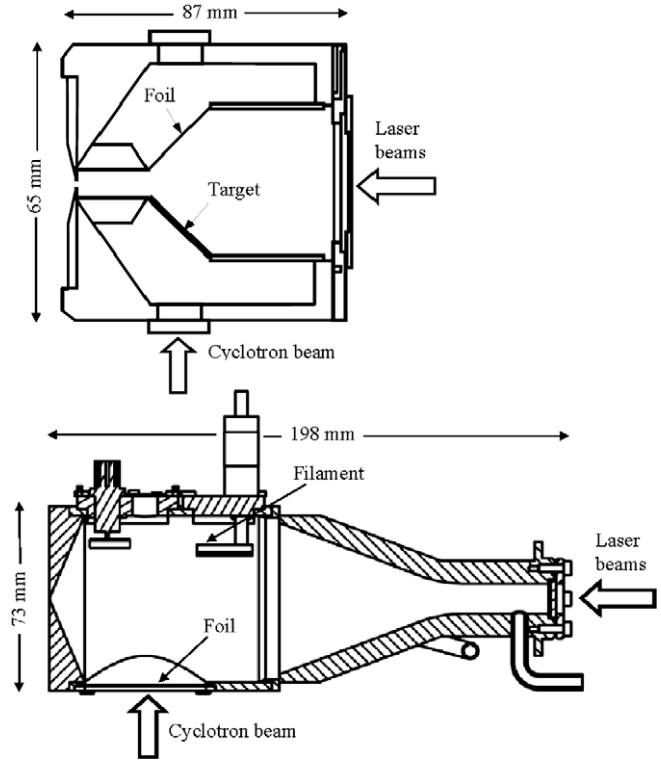

Fig. 1. Schematic view of the LISOL laser ion guide (top) and the ion guide designed in Jyväskylä (bottom).

At room temperature, the dimer ion becomes dominant at the gas pressures used in typical ion guide experiments and is formed at a rate $R = k[\rho]^2$, in which ρ is the number density of neutral gas atoms and the rate constant $k = 1.08 \times 10^{-31}$ cm^6 s^{-1} in helium [16], and $k = 2.5 \times 10^{-31}$ cm^6 s^{-1} in argon [17]. The lifetime for dimerization is given by $\tau = 1/(k[\rho]^2)$ and is ~0.33 μs at a helium pressure of 200 mbar, and ~0.14 μs in the equivalent pressure of argon.

One of the most important reactions on-line is that of three-body recombination of the type:

$$X^+ + e^- + B \rightarrow X + B, \tag{2}$$

where X^+ is an ion of interest or a buffer gas ion, and B is the buffer gas atom. Similarly, the reaction can be that of dissociative recombination (a two-body process):

$$B_2^+ + e^- \rightarrow B^* + B, \tag{3}$$

where B_2^+ is the buffer gas dimer ion. More generally, the rate constant for a two-body process ($X^+ + e^- \rightarrow X + h\nu$) is designated as α_2 (cm^3 s^{-1}). The three-body process of Eq. (2) has a rate constant α_3 (cm^6 s^{-1}). The total recombination rate coefficient α_{total} (cm^3 s^{-1}), referred to later as α, is the sum of these two processes:

$$\alpha_{\text{total}} = \alpha_2 + \alpha_3[\rho], \tag{4}$$

and is gas and pressure dependent [16]. For He^+ in He at 295 K, α_{total} is given by

$$\alpha_{\text{total}} = (1.12 \pm 0.05) \cdot 10^{-7} + (2.20 \pm 0.25) \cdot 10^{-27}[\rho]\text{cm}^3\ \text{s}^{-1}, \tag{5}$$

where the first term represents the two-body coefficient, the second term the three-body coefficient and $[\rho]$ the atomic number density of the gas (in cm^{-3}). In 200 mbar of helium gas at room temperature the total recombination rate coefficient $\alpha \sim 1.24 \cdot 10^{-7}$ cm^3 s^{-1}. In the case where argon is used as a buffer gas, there is no pressure dependence on the total recombination coefficient within the limits of experimental uncertainty [17], and α corresponds only to the two-body rate constant with a value of $1.07 \cdot 10^{-6}$ cm^3 s^{-1}. Within the literature we have found no experimental recombination rates measured for the metallic ions X^+ of interest. However, Bates and Khare calculated recombination rates for sodium ions in helium [18]. Their results indicated that so long as the recombining ion of interest is atomic, the chemical identity may not be very important in determining recombination rates. They suggest that recombination rates may vary inversely with the reduced mass of the ion and the neutral atom, therefore all atomic ions much heavier than He^+ would exhibit recombination rates ~50% of that of He^+ ions.

Recently, the role of impurities in the composition of high pressure noble gas plasmas has been discussed [19] and calculations have shown that trace impurities rapidly become the dominant carrier of charge. In that work the conversion of helium dimer ions was shown to take place via the charge exchange reaction with nitrogen:

$$He_2^+ + N_2 \rightarrow He_2^* + N_2^+, \tag{6}$$

with a reaction rate coefficient of 1.4×10^{-9} cm^{3}s^{-1}. The positive charge in the plasma is determined primarily by helium ions if the gas contains less than 1 part-per-million (ppm) of impurity. However, above this level the positive charge is completely determined by the nitrogen. Furthermore, this type of reaction is not restricted to nitrogen but applies to *any* impurity molecule and, as discussed by Morrissey et al. the chemical nature of the impurity simply depends on the operation of the gas cell [20]. Typical bimolecular charge exchange rate coefficients are $\sim 2 \times 10^{-9}$ cm^3 s^{-1}. In the work discussed in Section 4, performed under conditions of high impurity levels (~0.1 parts-per-million (ppm) [1]), the mean lifetime for a He_2^+ ion can be calculated simply using Eq. (7) of [1], $\tau \sim 1$ ms. If the impurities in the gas are reduced to a level of a few parts-per-billion (ppb) then the mean lifetime of He_2^+ increases to $\tau \sim 100$ ms. The fate of the dimer ions strongly depends on the impurity level within the gas cell and the extraction time from the cell.

The initial production rate of ion-electron pairs in the buffer gas following the passage of a primary beam is governed by the primary beam intensity I (pμA), the energy loss of the beam ΔE (eV) in the stopping volume V (cm^3) and the mean ionization energy needed for the production of one ion-electron pair, W (41 eV for helium and 26.4 eV for argon) [3]. The ionization density rate Q (ion-electron pairs cm^{-3} s^{-1}) can be written as

$$Q = 6.25 \cdot 10^{12} \frac{I}{A} \frac{dE/dx}{W}, \tag{7}$$

where (dE/dx) is the linear energy loss of the ion (eV/cm) and A is the beam spot area (cm^2). In our work involving yttrium filament atoms (Section 4), the energy loss of a 30 MeV primary beam of $^4He^{2+}$ through the ion guide at a helium pressure of 200 mbar is 7.94×10^3 eV/cm. The beam was collimated to a diameter of 8 mm and was kept at a fixed intensity of 10 pnA. The ionization density rate Q is therefore calculated to be 2.4×10^{13} pairs/cm^3 s. As the beam passes through the ion guide the charge density $n = n_{\text{ion}} = n_{\text{electron}}$ evolves in time according to the expression [21]:

$$\frac{dn}{dt} = Q - \alpha n^2. \tag{8}$$

This expression has the solution:

$$n(t) = n_0 \frac{e^{2t/\tau} - 1}{e^{2t/\tau} + 1}, \tag{9}$$

in which the equilibrium density n_0 is given by

$$n_0 = \sqrt{\frac{Q}{\alpha}}, \tag{10}$$

and the characteristic time τ for the plasma to reach an equilibrium is expressed as

$$\tau = \frac{1}{\sqrt{Q\alpha}}. \tag{11}$$

Using the value for Q and α given above results in an equilibrium density of 1.4×10^{10} pairs/cm^3 and a characteristic time to reach this value of 580 μs. This is approximately a factor of two shorter timescale than the charge-transfer lifetime of He_2^+ ions to impurities under the present experimental conditions.

It is generally known that ionized buffer gas can have fast charge transfer to atoms depending on the availability of final states of the product ions that make the reaction nearly energy resonant, i.e. very slightly exoergic. The two predominant charge-transfer mechanisms in the case of helium are the thermal energy charge-transfer reaction:

$$He^+ + X \rightarrow (X^+)^* + He + \Delta E, \tag{12}$$

and the Penning ionization reaction:

$$He^*(2^3S) + X \rightarrow (X^+)^* + He + e^- + \Delta E, \tag{13}$$

where X is the ground state of the atom of interest, $(X^+)^*$ is an excited state of the singly-ionized ion and ΔE is the energy defect, calculated by subtracting the final energy from the energy of the colliding system. In a similar manner to that of reaction (12), the helium dimer He_2^+ ion can charge exchange with the atom of interest resulting in the formation of two helium atoms. Investigations of reaction (12) have shown that the charge-transfer cross section is largest for $0 < \Delta E < 0.4$ eV [22,23]. Furthermore, the authors of [23] conclude that contrary to the case of charge-transfer reactions there appears to be no tendency for which the energy defect must be small in a Penning reaction. In fact, the cross section for reaction (13) increases with the energy defect, becoming largest for the production of the metal-ion ground state. In all cases where levels of the product metal ion are accessible to excitation by a Penning reaction, excitation occurs. The triplet metastable level is given in Eq. (13) as it has been observed to have the highest population density [24] and is fed rapidly from the conversion of singlet metastable atoms via collisions with electrons [25].

Unfortunately, few charge-transfer reaction rates for metallic ions are found in the literature and those measurements that have been performed are primarily motivated by the study of gas discharge lasers [22,24,26–33]. In Refs. [31,32] cross sections of Penning ionization and charge transfer were measured for He^+-Cd and He^+-Zn, respectively. In both cases the cross sections are almost identical to each other within a factor of 1.5. Typical charge-transfer rate coefficients for resonant transitions are of the order of $10^{-9} - 10^{-10}$ cm^3 s^{-1}.

Finally, it is informative to mention the role of the metastable atomic density within the gas cell. Following the initial ion-electron pair creation caused by the passage of the primary beam and subsequent fast dimerization, 70% of the He_2^+-electron recombination leads to the $He^*(2^3S)$ metastable state via the three-body recombination reactions [25]:

$$He_2^+ + e^- + e^- \rightarrow He_2^* \rightarrow He^*(2^3S) + He + e^-, \tag{14}$$

and

$$He_2^+ + e^- + He \rightarrow He_2^* + He \rightarrow He^*(2^3S) + He + He. \tag{15}$$

The rate coefficients for reactions (14) and (15) are $k = 0.7{*}4 \times 10^{-20}$ cm^{6}s^{-1} and $k = 0.7{*}5 \times 10^{-27}$ cm^6 s^{-1}, respectively. Using the equilibrated number density of electrons ($n_e = 1.4 \times 10^{10}$ cm^{-3}) given by Eq. (10) and the number density of helium atoms at 200 mbar pressure ($n_{He} = 5.3 \times 10^{18}$ atoms/cm^3) the lifetimes for reactions (14) and (15) are calculated to be $\tau \sim 182$ ms and $\tau \sim 4$ ms, respectively. It is most likely that reaction (15) is dominant as the concentration of neutral helium atoms is $\sim 10^8$ times larger than the concentration of electrons. With 70% of the He_2^+ ions being converted to metastable atoms then the density of metastable atoms in the buffer gas can be calculated to be $\sim 9.8 \times 10^9$ cm^{-3}. In the conditions of the present work, the lifetime for reaction (15) is rather similar to the survival time of helium dimers against charge exchange with impurities (reaction (6)) and therefore these processes compete with each other. On the other hand, with a much cleaner gas cell one would expect that the metastable formation would dominate as the main loss mechanism for helium dimer ions.

A variety of loss mechanisms for the metastable He_m^* atoms are discussed in [34], along with associated rate coefficients. Here we only mention the dominant loss mechanism, defined by the shortest timescale:

$$He_m^* + He \rightarrow He + He, \tag{16}$$

with an associated two-body rate coefficient of $k = 6 \times 10^{-15}$ cm^3 s^{-1}. The timescale for this reaction at a helium pressure of 200 mbar is calculated to be $\tau = 31$ μs.

In analogy with helium, there exists two argon metastable levels lying close to each other, the $(3p^5 4s)^3P_2$ level and the $(3p^5 4s)^3P_0$ level, at 11.55 and 11.72 eV above the ground state, respectively. The $^3P_0$ level is stated to be populated a fraction of 10–20% of the $^3P_2$ level [35]. In the literature we have found that the metastable levels are populated in discharge experiments either via electron impact excitation from Ar atoms or radiative recombination of singly-charged Ar ions [34]. We have not found similar metastable production reactions, however, to those involving the helium dimer ions (reactions (14) and (15)), and assume here that the equivalent reactions are in fact possible for Ar_2^+ and occur on a fast timescale. In analogy with He_m^* atoms, a variety of loss mechanisms exist for the Ar_m^* atoms [34], dominated by the three-body reaction:

$$Ar_m^* + 2Ar \rightarrow Ar_2^* + Ar, \tag{17}$$

with an associated rate coefficient $k = 1.4 \times 10^{-32}$ cm^6 s^{-1}. The number density n_{Ar} of Ar atoms at a pressure of 200 mbar is 5.3×10^{18} atoms cm^{-3} and therefore the timescale for this reaction is calculated to be $\tau \sim 3$ μs. We note that the main loss mechanism of the helium metastable atoms result in ground state helium atoms, whereas in reaction (17) the formation of an excited diatomic Ar molecule occurs. If we suppose that the $^3P_2$ level is the dominant metastable state in the Ar buffer gas then the corresponding diatomic molecular state is that of the $Ar_2^*(3\Sigma_u^+(0_u^-, 1_u))$ level [36], with a lifetime of a few μs. Because reaction (17) is resonant, the reverse reaction is possible:

$$Ar_2^* + Ar \rightarrow Ar_m^* + 2Ar, \tag{18}$$

and therefore an equilibrium level of Ar metastable atoms is achieved.

4. On-line studies with filament-produced yttrium atoms

The results described in the following sub-sections have been obtained using the LISOL laser ion guide. In our previous article we discussed the first studies on gas phase chemistry using this ion guide, performed in March 2006, following which a contami-

nating leak was found in the gas feeding line [1]. Immediately following this experiment, the effects of the passage of a 30 MeV primary beam of $^4He^{2+}$ through the ion guide, presented here, were obtained and therefore the results also contain contaminating impurities. In this work, an yttrium filament of thickness 3.75 mg/cm^2 cut into a bowtie configuration with a diameter of 3 mm at the narrowest part, was mounted in the ion guide towards the rear. The laser light enters the guide longitudinally through a sapphire window and the primary beam passes through the gas cell perpendicular to the extraction axis at ~48 mm from the exit nozzle.

4.1. Equilibrated yields – information on laser ionization, molecular formation and recombination

In order to investigate the effect of the primary beam on both the neutral yttrium filament atoms and the laser-ionized yttrium ions, the primary beam and the laser beams were pulsed using a timing sequence with TTL signals from the JYFLTRAP control program [37]. The ion signal, detected on a set of channel plates mounted downstream from the focal plane of the IGISOL mass separator was fed into a multichannel analyzer (MCA) with a time resolution of 655.36 μs per bin. The time profiles of $^{89}Y^+$, YO^+ and $YO^+(H_2O)_3$ are shown in Fig. 2.

A total cycle time of 4 s was employed by the control program. The laser radiation was pulsed on from 1.5 to 3 s and again from 3.5 to 4 s. The cyclotron beam was on from 1 to 2.5 s. These periods are represented by horizontal bars above the time axis (see figure caption for details). Time profiles were also recorded for all the hydrate attachments that have been discussed in [1] ($YO^+(H_2O)$, $YO^+(H_2O)_2$ and $YO^+(H_2O)_4$) however these have not been shown in Fig. 2 to maintain clarity.

The filament was continuously heated during this work. The structure seen in Fig. 2 just after the initial start time can be ignored as it is an effect of the JYFLTRAP program and is a "wrap-around" of the data at the end of the scan being written to the file. Fig. 3 shows a comparison of the saturated yields of yttrium and all associated molecules under the different conditions, namely "laser only", "beam only" and "laser and beam". Additionally the effect of the laser ionization during the primary beam period can be extracted by subtracting the yield obtained in the "beam only" period from that of the "laser and beam" period. The sequential formation times for the different molecules are taken from Table 4 in Ref. [1] and are indicated on the top of the figure.

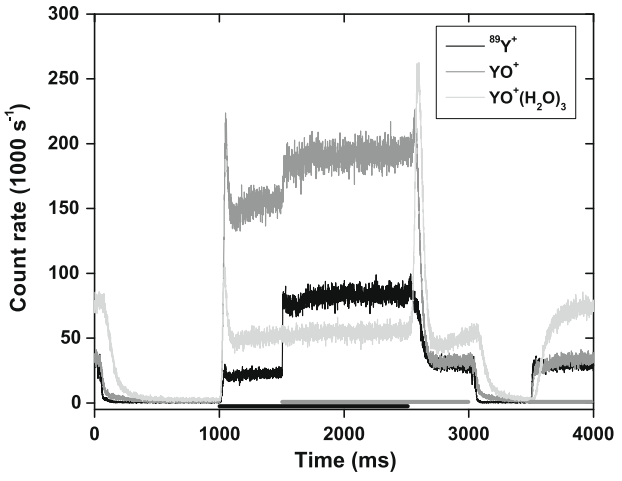

Fig. 2. Time profiles for Y^+, YO^+ and $YO^+(H_2O)_3$ showing the influence of the primary beam passing through the ion guide. The black (grey) line above the time axis indicates the period when the accelerator (laser) beam was on.

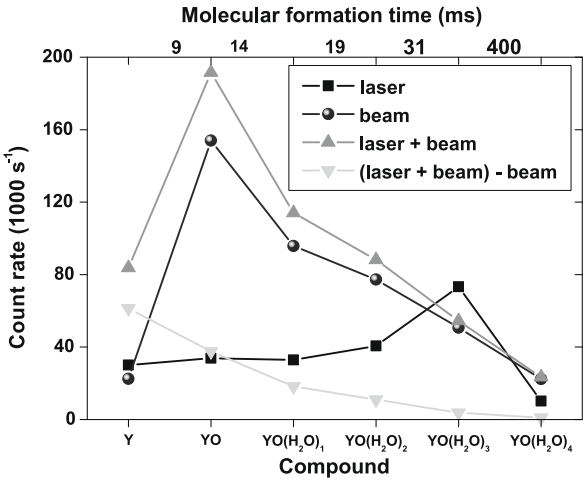

Fig. 3. A comparison of the saturated yields for yttrium and associated molecules. The timescale associated with molecular formation is shown on the upper *x* axis, taken from Table 4 of [1].

During the "laser only" period the relative trend in yield closely follows that seen in the off-line conditions summarized in Fig. 11 of [1]. The main contribution to the yield comes from $YO^+(H_2O)_3$ which can be explained via the time evolving sequence of hydrate additions to YO^+ and the long evacuation time of the ion guide (~100 ms along the laser axis). In contrast, when the primary beam is turned on the dominant molecule is shifted to YO^+ and the yield drops steadily for the hydrate additions. Using the rate equations that describe the molecular formation processes given by Eq. (17) of [1] and the molecular formation times from Table 4 of the same reference, we have estimated that the dominant molecule formed during evacuation from the beam region would be $YO^+(H_2O)_2$, assuming an initial condition of 100% yttrium atoms. The addition of the primary beam complicates this picture by introducing an ionization mechanism which is non-selective, unlike that of laser ionization. Also, the beam-related processes are not confined to the beam interaction region but are in equilibrium as the ion-electron pair density evolves towards the exit hole. These processes may include a continuous break-up of hydrate molecules in the channel of the ion guide which feeds the YO^+ yield. Although the beam energy deposited into the ion guide is high enough to decompose YO^+ into atomic yttrium ions this is not reflected in the "beam only" data because the reformation of YO^+ due to reactions with impurities is too strong. A similar overall trend is observed in the case when both lasers and beam are on.

The effect of the laser ionization in the presence of the primary beam is indicated in Fig. 3 by the light grey symbols. The strongest laser enhancement is observed for yttrium, monotonically decreasing for each subsequent molecule until the yield is dominated by beam ionization in the case of $YO^+(H_2O)_4$. The increase in the atomic yttrium ion fraction compared to off-line conditions is associated with an increase in the number of neutral yttrium atoms in the laser beam path, most likely caused by the decomposition and recombination of molecular species during evacuation from the guide. From the molecular formation times indicated in Fig. 3, a typical timescale for the effective laser ionization in the presence of the primary beam is ~10 ms. This can be compared to the timescale associated with the strongest laser effect under off-line conditions (in which YO^+ $(H_2O)_3$ is the main contributor), ~100 ms, indicating the limited effective volume within which laser ions survive in the presence of a plasma.

The dominance of recombination compared with formation of molecular compounds via laser ionization of atomic yttrium is highlighted in Fig. 4, which shows the time profile of YO^+ $(H_2O)_3$

with and without laser ionization. The laser effect in the upper panel is calculated by subtracting the two graphs in the lower panel. While the cyclotron beam is on, no formation of molecules via laser ionization of atomic yttrium is observed. Approximately 50 ms after the primary beam has been turned off, the plasma has been evacuated and the laser ion signal starts to increase, reflecting the survival of laser-produced yttrium ions and related molecules against recombination. It is noticeable that the rise time of the laser effect during the presence of the striking beam-related peak is faster than that of typical off-line conditions which are represented following the brief 0.5 s laser off period, following which the laser is turned on again at 3.5 s. Further details in connection to such an effect will be addressed in Section 4.3.

4.2. Dynamic processes – information from the atomic and molecular time profiles

The saturated yields observed within the different periods of the laser and primary beam provide information on the equilibrated processes within the ion guide. Additionally, the time distribution profiles can also be used to understand the dynamic processes. In the initial period when the cyclotron beam first passes through the gas cell the buffer gas is ionized almost instantaneously, along with the yttrium filament atoms and corresponding molecules. All species reach a peak (less noticeable in yttrium) at the same time, ~50 ms after the beam has been turned on (Fig. 2). This common delay is associated with the gas flow evacuation from the ion guide and has been simulated using a flow model based on the COMSOL software package [38]. A complete description of the model is detailed in [39] and is only briefly discussed here. The flow of atoms in the gas is governed by the macroscopic motion of the gas flow. Additionally a random diffusion process can be taken into account according to the model described in [40,41]. During a time step Δt the particle travels a distance of:

$$\Delta \boldsymbol{x} = \boldsymbol{v}(\boldsymbol{x})\Delta t + \boldsymbol{x}_D, \tag{19}$$

where $\boldsymbol{v}$ denotes the macroscopic gas velocity and $\boldsymbol{x}_D$ a random diffusion step calculated from standard diffusion theory. From the COMSOL software package a velocity map containing the coordinate pair (r,z) and the velocity vector (v_r,v_z) in cylindrical coordinates was imported into *Mathematica* [42]. With the known velocity profile, a routine was written to numerically integrate Eq. (19) from a chosen starting point within the ion guide in order to monitor the trajectory of a single ion.

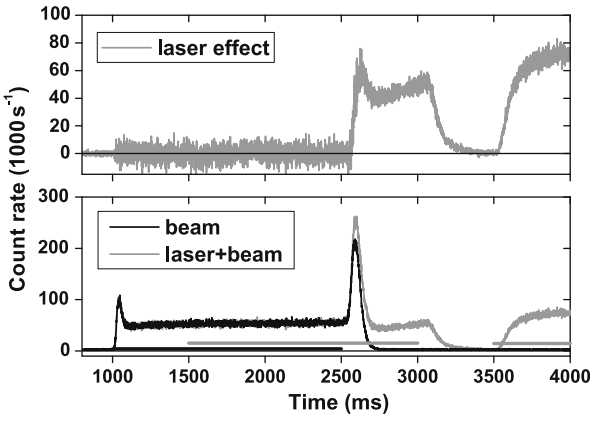

Fig. 4. The time profile of $YO^+(H_2O)_3$. The black (grey) line above the time axis indicates the period when the accelerator (laser) beam was on. The top panel shows the effect of the laser ionization by subtracting the two graphs in the lower panel.

In this particular instance the gas flow was inverted in the simulation, corresponding to a time-reversal according to Eq. (19). The initial ion distribution was chosen to start from a random position within the nozzle area of the gas cell. The time-reversed trajectories were followed for 50 ms and the final position was recorded. Any ions that hit a wall were neglected. The result of a simulation of 1000 ions is shown in Fig. 5. The two horizontal lines mark the position of the beam entrance window. The typical trajectory of a single ion track can be seen and it is clear that the majority of ions are indeed created in the beam interaction region.

The effect of laser ionization on the time profile of atomic yttrium in the presence of the equilibrated plasma, seen in Fig. 2 when the lasers are turned on at 1.5 s, is shown in more detail in Fig. 6 (filled triangles). The background due to the primary beam has been subtracted in order to compare with the off-line data taken from 3.5 to 4 s in Fig. 2 (spheres). A delay of ~5 ms occurs before the effect of the lasers is noticeable. This is caused by a time delay in the laser shutter and is not related to the time-of-flight of the ions. The exponential growth curve fitted to the $^{89}Y^+$ data provides valuable information on the effective volume from which

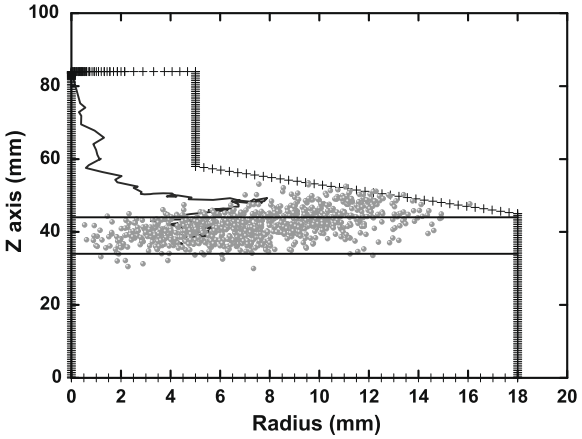

Fig. 5. A time-reversed gas flow simulation in which ions are randomly created in the nozzle region of the ion guide, located at ~84 mm along the Z axis. The ions are allowed to travel for 50 ms at which point their final position is recorded.

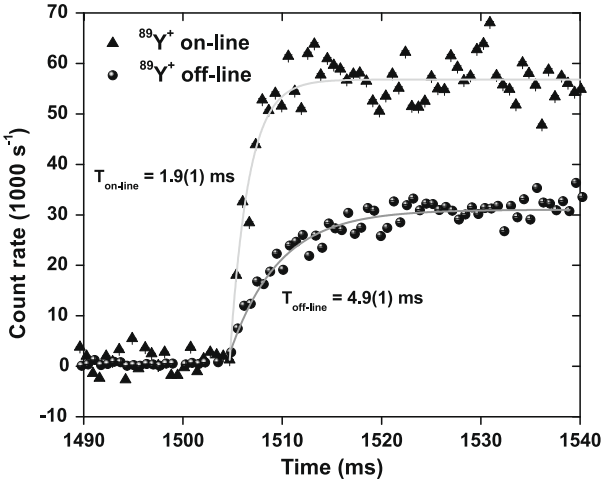

Fig. 6. The Y^+ time profile when the lasers enter the ion guide at t = 1.5 s, in the presence of the primary ions from the beam (solid triangles). For comparison we show the off-line data shifted in time from the same data set (Fig. 2) (spheres). Both data sets are fitted using a simple exponential growth curve.

laser-produced ions can be successfully extracted in the presence of the plasma. A fit value of $\tau = 1.9(1)$ ms corresponds to a sum of the conversion of Y^+ ions to molecules and losses due to the effect of the plasma density. We can therefore estimate the time constant associated with the plasma effect, $\tau_{plasma} = 1/(1/\tau - 1/\tau_{mol}) = 3.1$ ms, where $\tau_{mol} = 4.9(1)$ ms, extracted from the fit of the off-line data. By combining this saturation time with the conductance of the exit nozzle ($112\ cm^3\ s^{-1}$) one can estimate the effective laser ionization volume for Y^+ in the presence of the plasma. This is calculated to be $0.35\ cm^3$, only ~0.7% of the total volume of the ion guide and 64% of the effective ionization volume of that calculated in the presence of molecular formation alone. We note that studies by the LISOL group, University of Leuven, indicated that even at time scales around 5 ms, recombination losses of the ion of interest start to become important once the ion-electron density is above $10^7 - 10^8\ cm^{-3}$ [3].

For comparison, we also show the off-line data shifted in time to correspond with the initial increase in the on-line data. Not only are the different time scales illustrated, reflecting the different effective volumes from which laser-produced ions are evacuated, the increase in the yttrium ion yield in the presence of the effects of the primary beam can also be seen. This has already been discussed with reference to Fig. 3.

In the direct beam interaction region the evolution of the ion-electron pair density is governed by Eq. (8). When the beam is turned off, or in this case, when the gas flow moves the ion-electron pairs out of the beam region towards the nozzle, the ion-electron density is no longer in equilibrium. Recombination becomes the dominant process and the density of ions and electrons evolve in time as

$$n(t) = \frac{n_0}{1 + \alpha n_0 t}, \tag{20}$$

where n_0 is the initial density (given by Eq. (10)). The evacuation time of a 6 mm cylinder along the ion guide axis (the laser ionization zone) from the beam region to the exit nozzle is ~50 ms. During this time the ion-electron density reduces from an initial value of 1.4×10^{10} pairs/cm^3 to a value of 1.6×10^8 pairs/cm^3 according to Eq. (20). If we assume that the time constant τ_{plasma}, determined from the increase in the $^{89}Y^+$ signal when the lasers are turned on (Fig. 6) is due to recombination caused by the electron density in the nozzle region, then we arrive at a contradiction. The electron density needed to satisfy the value of $\tau_{plasma} = 3.1$ ms is $2.2 \times 10^9\ cm^{-3}$, a factor of ~14 higher than that estimated from the direct beam-related density transported by gas flow.

We have considered additional sources of electrons in order to explain the discrepancy, for example via metastable–metastable collisions or non-resonant photo-ionization from vacuum-ultraviolet (vuv) photons which are created as a charged particle loses its energy as it passes through the gas. In the latter case, we have explicitly shown that the non-resonant ionization cross section is too small for direct ionization [39]. Additionally, due to the low metastable densities in the nozzle region it is very unlikely that we have a source of electrons with a density considerably higher than that associated with the plasma density.

On the other hand, it is possible that laser ionization is indeed working deeper within the ion guide however the photo-ions are not effectively transported to the nozzle region due to the plasma-generated field within the gas cell. This effect could explain the fast saturation time seen in Fig. 6 and the difference in rise times in the $YO^+(H_2O)_3$ profile of Fig. 4. It is important to note that we are not discussing the effects of adding an external electric field in the gas cell. The motion of the produced plasma in an ion guide system is governed mainly by ambipolar diffusion and gas flow. The electric field associated with the plasma can be described as

$$\boldsymbol{E} = \frac{D_i - D_e}{\mu_i + \mu_e} \nabla \ln(n) \sim -\frac{k_B T_e}{q} \nabla \ln(n), \tag{21}$$

where μ and D are constants for the mobility and the diffusion of the electrons and ions (He^+ and Ar^+ in our case), respectively, and T_e the temperature of the electrons. Earlier work calculating the electron energy distribution functions (EEDF) has shown that the temperature of the bulk electrons in helium gas remains at 300 K even at very high beam intensities (up to 10^{16} He^{++} pps cm^{-2}) [43]. On the other hand, if Ar is used as a buffer gas, only at low beam intensities (less than 10^{12} pps cm^{-2}) is a similar electron temperature maintained. For beam intensities exceeding this value, the primary projectiles transfer a sufficient amount of energy to the electrons such that the bulk temperature increases, approaching 0.4 eV at 10^{18} pps cm^{-2}.

As an example, in the following we discuss the geometry of the LISOL laser ion guide evacuation channel (10 mm in diameter, 26 mm in length) using a simple approach to determine the ion transport in a tube. We note that the exit hole itself is not discussed due to uncertainties arising from the plasma density distribution and the need for additional gas flow modeling. The plasma density in the channel is defined by the recombination process of Eq. (20) and the gas flow velocity which follows the $v = v_0(1 - (r/r_0)^2)$ rule, where v_0 is the gas velocity on the axis of the channel and r_0 the channel radius. For simplification we ignore the role of diffusion of the plasma distribution. We can then write the expression for the plasma density $n(z,r)$ as

$$n(z,r) = \frac{n_0 v_0 (r_0^2 - r^2)}{v_0(r_0^2 - r^2) + \alpha n_0 z r_0^2}, \tag{22}$$

where n_0 is the plasma density in the primary beam area.

From Eq. (21) and (22) we calculate the electric field produced by the plasma flow in the channel, assuming an electron temperature of 300 K. Fig. 7 illustrates the radial component of the electric field as a function of the radial position across the channel at an extraction axis position of $z = 1.5$ cm. As a function of the extraction axis (z), the radial component is rather constant between $z \sim 0.2$ cm and the exit nozzle, decreasing rapidly close to the primary beam area. The knowledge of the electric field and gas velocity allows one to calculate trajectories of individual ions under study. For illustration, the plasma density distribution and a sample of calculated ion trajectories are shown in Fig. 8. We note that these ion trajectories refer to the species of interest, rather than the buffer gas ions themselves. It is of interest to estimate the effect of the electric field on the ion velocity in comparison to the gas flow

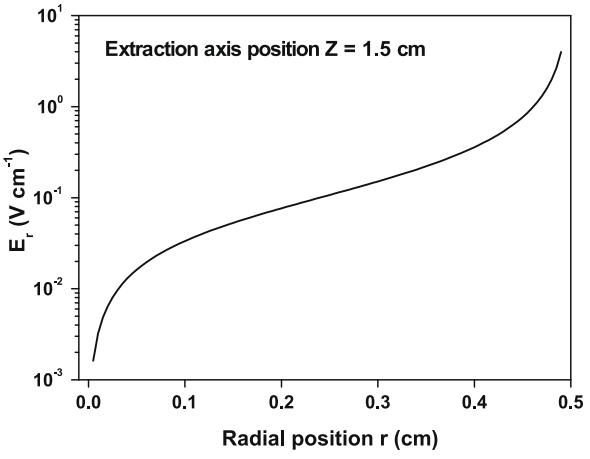

Fig. 7. The radial component of the plasma-generated electric field as a function of radial position from the extraction axis of the LISOL ion guide channel. Within the channel the component is rather constant as a function of the extraction axis z.

velocity. For an ion moving along the extraction axis at a radius r of 2 mm, the velocity due to gas flow is ~130 cm s^{-1}. The electric field at this radius is ~0.076 V cm^{-1}. By combining this with the ion mobility in 100 mbar helium pressure (~200 cm^2/Vs) one can calculate the velocity to be ~15 cm s^{-1}. Therefore, the effect of the generated electric field is ~10% of that due to the gas flow.

The transmission efficiency ϵ of the exit channel was estimated from the ratio of the transmitted ions to the total number of ions injected along the cross sectional area of the channel entrance ($z = 0$ cm). For a continuous beam the transmission as a function of initial plasma density is illustrated in Fig. 9, comparing the behaviour for He and Ar. Following the discussion of gas cell processes in Section 3 we fix the recombination coefficient of an ion of interest to be 5×10^{-8} cm^3 s^{-1}, ~50% of the recombination coefficient for the He^+ ion. The evacuation efficiency in He for an initial density of 10^{10} pairs/cm^3 is calculated to be $\epsilon = 0.043$ without recombination, decreasing to $\epsilon = 0.011$ including recombination.

The essential difference in the behaviour of the transmission efficiency in the He and Ar channel can be explained by the larger neutralization coefficient and lower gas velocity of Ar compared to He. The neutralization process of the Ar plasma occurs primarily in the beginning of the plasma travel in the channel and the plasma density gradient is high only close to the beam region. The plasma in most of the channel has a relatively low density and, as a result, the neutralization of the studied ion is not very probable. In the case of He, the gas flow rate is higher and the neutralization rate of the plasma is lower, thus a higher density of plasma is delivered deeper in the channel towards the exit nozzle. The high neutralization rate of the studied ion (see the difference in Fig. 9 with and without neutralization) is an indication of the higher density of electrons further from the direct beam area. We briefly note that the role of impurities can further complicate such a picture depending on the impurity level within the gas cell (see Eq. (6) for an example of a charge exchange process). If the impurity level is high then the buffer gas ions can transfer their charge to the impurity atoms. A complex plasma arises if it is composed of more than one species which has different ion mobilities.

The transport efficiency and evacuation time for ions with randomly distributed starting positions inside the channel can also be estimated. This corresponds to the situation in which laser ionization occurs in the presence of the beam-generated plasma. The initial positions of successfully transmitted ions illustrates the effectively evacuated volume as shown by the scattered points in Fig. 8. It is clear that close to the nozzle region, a larger cross sectional area of the channel is accessible. It is of interest to simulate the response of the ion count rate to the laser ionization process. Fig. 10 compares the count rate as a function of time for the case without any beam-related plasma, a plasma density of 10^{10} pairs/cm^3 and the same density but including the effect of recombination of the transported ions (Eq. (20)). It should be noted that we ignore the losses due to molecular formation. A strong reduction of the count rate in the presence of the plasma occurs, directly attributed to a reduced transmission efficiency of ions to the exit nozzle region. The effect of recombination reduces the transport efficiency (and thus count rate) but not as strongly as the effect of the plasma-generated field in the gas cell. The rise times of the simulation data in Fig. 10 can be qualitatively compared to the experimental data shown in Fig. 6, in which the presence of a plasma results in a shorter time needed to reach saturation.

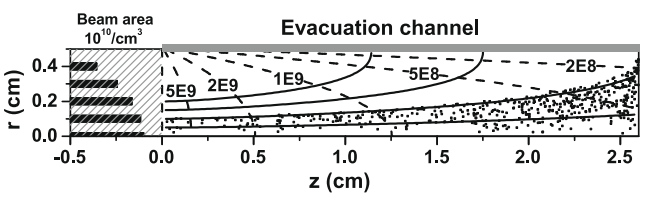

Fig. 8. Plasma density distribution in the evacuation channel (dashed lines) and ion trajectories for different initial radial positions (solid lines). The randomly scattered points are the starting positions of those ions which are successfully transmitted through the channel, moving from the left towards the right in the figure. The gas flow velocity is illustrated by horizontal bars and corresponds to $v_0 = 155$ cm s^{-1} and an evacuation flow rate $Q = 81$ cm^3 s^{-1}. The pressure in the simulation was $P = 100$ mbar.

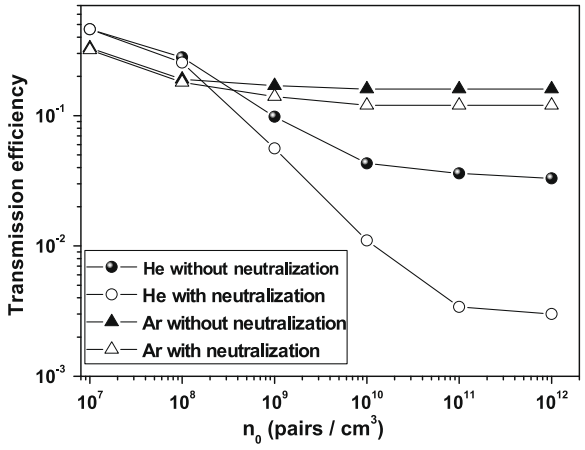

Fig. 9. The laser ion guide channel transmission efficiency as a function of initial plasma density for an ion of interest in He and Ar buffer gases. Also shown is the effect of neutralization of the ion of interest.

4.3. Possible origins of the primary beam-related spikes

Perhaps the most striking feature of the time profile data of Fig. 2 are the two pronounced primary beam-related peaks, seen most evidently in $YO^+(H_2O)_3$, which are correlated to the period when the primary beam is first turned on and again when it is turned off. Apart from atomic yttrium, these peaks are also strongly apparent in the profiles of all other molecules, albeit to a somewhat lesser extent than that of $YO^+(H_2O)_3$. This is illustrated in Fig. 11 in which the time profile of Y^+ and all molecules are shown individually. It is rather interesting to note that unlike the similar arrival time of the atomic ions and molecules from the beam region after the beam has been turned on (50 ms), the peaks associated with the turning off of the primary beam do not arrive

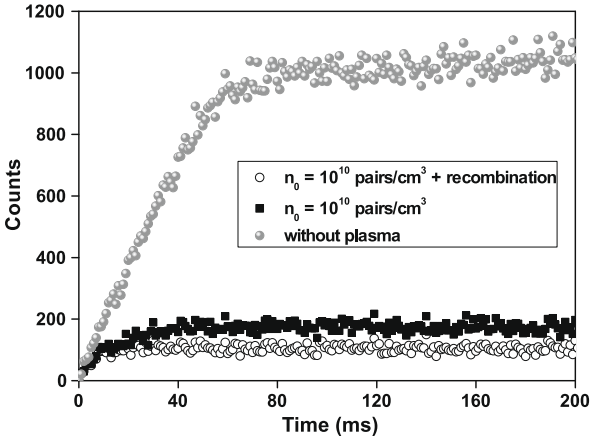

Fig. 10. The time profile associated with the response to the beginning of the laser ionization process. The data sets correspond to the expected profile without plasma (spheres) and a plasma density of 10^{10} pairs/cm^3 with and without recombination of the transported ions (open circles and solid squares, respectively).

at the same time. In each case however there is an approximate period of 50 ms following turn off of the beam at 2.5 s while the count rates remain in equilibrium. This agrees with the evacuation time of the plasma from the beam region. The time structure describes a transition from a regime dominated by on-line conditions in which the YO^+ molecule is most abundant, to that of off-line conditions dominated by molecular formation and laser ionization in which the most abundant molecule is that of $YO^+(H_2O)_3$ [1].

The origin of the beam-related spikes is not a simple matter to address and firm conclusions cannot be made with the limited available experimental information. However, in the following we present two independent approaches in order to illustrate that such phenomena may be qualitatively reproduced. In the first approach, a detailed effort has been made to simulate the time evolution of the ion densities within the gas cell, incorporating several processes that lead to the creation and destruction of the atomic and molecular ions during evacuation from the gas cell. In the following we provide only an outline of the simulation which highlights the competition of different processes within the ion guide.

Fig. 12 illustrates the basic framework of the simulation in which the ion guide is treated as three separate volumes, A, B and C. Volume A represents the feeding volume of atoms, molecular atomic species and impurities into volume B, the beam interaction zone. For a heated filament evaporating yttrium atoms, the saturation number density in volume A is estimated and converted into a feeding rate towards volume B via the evacuation time of A. This is estimated to be ~380 ms via the conductance of the exit nozzle. The feeding rate determines the atomic saturation density in volumes B and C before the primary beam is turned on. The dimensions of the ionization region of volume B are defined by the diameter of the collimator (8 mm). A gas flow simulation in the manner of that discussed in Section 4.2 has been performed, taking an initial distribution of ions along the two boundaries of the beam interaction region. Including diffusion, the evacuation time of volume B is estimated to be t_{evac} ~44 ms. Ions are finally extracted following evacuation through volume C in a timescale of ~55 ms.

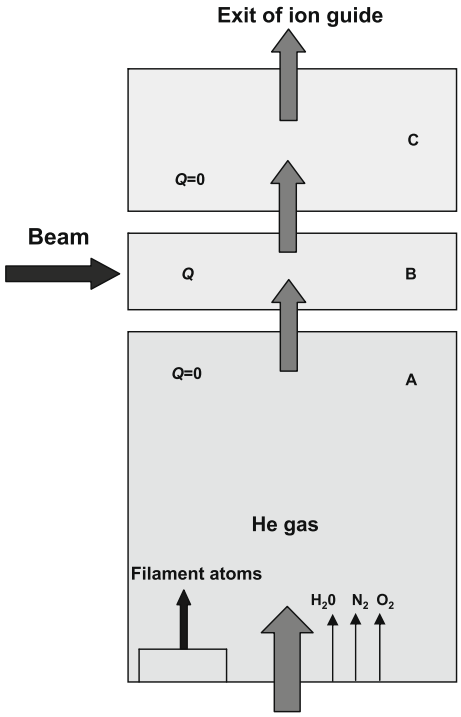

Fig. 12. Schematic of the gas cell separated into three volumes. Volume A feeds atoms, molecules and impurities into volume B which is defined as the beam interaction zone. The ions are finally evacuated from the ion guide after passing through volume C.

In order to estimate the production rate of yttrium atoms from the filament an off-line measurement was performed within a bell jar filled with 200 mbar of helium. A filament of equivalent thick-

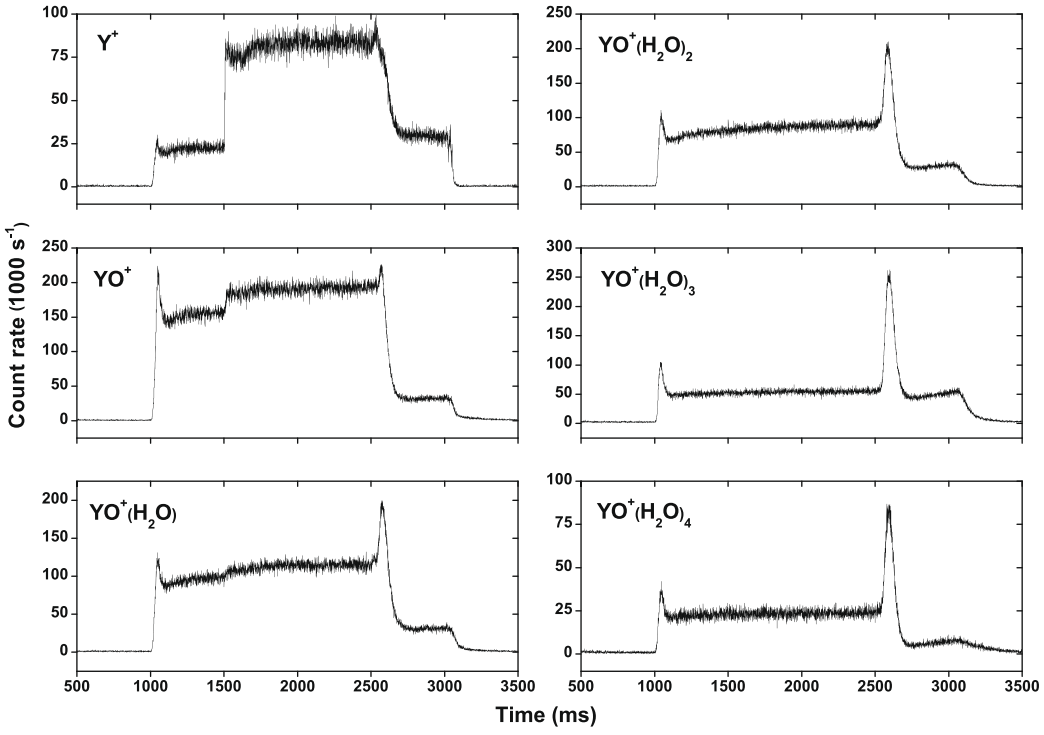

Fig. 11. Time-of-flight profiles for Y^+ and all associated molecules when the primary beam is pulsed on at 1 s and off at 2.5 s. Note that the laser is turned on at 1.5 s.

ness as that used in the ion guide was resistively heated at the same current (4A) and was weighed before and after. In 1080 s the foil lost 0.1 mg, a rate of 6.3×10^{14} atoms/s. By including the volume of the ion guide, ~54 cm^3, a normalized production rate of 1.2×10^{13} atoms/cm^3 s is calculated. The initial saturation density of yttrium atoms within volume A can be estimated as follows:

$$[Y] = \frac{n}{k'[M] + \lambda}\left(1 - e^{-(k'[M]+\lambda)t}\right). \quad (23)$$

In this equation, n is the production rate of yttrium (1.2×10^{13} atoms/cm^3 s), k' (cm^3 s^{-1}) is the molecular reaction rate coefficient for the atom (not to be confused with k which has been defined in Eq. (6) of Ref. [1] as the reaction rate coefficient for the ion), λ (s^{-1}) is the inverse of the evacuation time of volume A, and [M] and [Y] are the impurity and yttrium atom concentration, respectively. The solution of Eq. (23) defines an upper limit to the yttrium concentration as losses through diffusion are not taken into account.

The impurity level in the March 2006 off-line experiment was estimated to be ~0.1 ppm [1]. However, we did not have access to a certified admixture of impurities in the bottle of high-purity helium gas (grade 6.0, 99.9999%) and therefore a similar admixture as discussed in [44] has been used, scaled to match our off-line impurity level measurement. By including only water and oxygen contaminants, an overall impurity level of 0.06 ppm in 200 mbar of helium results in an impurity concentration [M] of $\sim 3.2 \times 10^{11}$ atoms/cm^3. The reaction rate constants for neutral atom-molecule bonding are approximately two orders of magnitude lower than for ions and thus the timescale for the formation of an atom-molecule adduct will be two orders of magnitude longer [45]. Following the discussion in our earlier work [1], the reaction rate coefficient k' for the neutral yttrium atom-molecule formation and subsequent hydrate additions is therefore assumed to be 4.1×10^{-12} cm^3 s^{-1}.

The initial saturated densities of neutral YO and associated hydrate additives are estimated in a similar manner. All densities of interest are subsequently converted to feeding rates into the ionization volume. The feeding rates become the initial production rates of all species in volume B, and the differential equations are solved once more to provide the initial estimates of all densities within the ionization volume prior to the "beam on" period. When the primary beam enters the gas cell the processes discussed in Section 3 start to play an important role, including molecular ion formation as discussed in [1]. The primary beam is a non-selective ionization mechanism and therefore can ionize all neutral species within the ion guide.

The simulation follows a set of differential equations representing competing processes (note these are not exhaustive, for example we do not include Penning ionization or laser ionization). In this manner, the evolution of an ion X^+ within the helium gas can be studied as follows:

$$\frac{d[X^+]}{dt} = Q_X + a[He^+][X] + b[H_2O^+][X] + c[O_2^+][X] - \alpha[X^+][e^-] - k[H_2O][X^+] - k'[O_2][X^+] - \lambda_{evac}[X^+]. \quad (24)$$

The first four terms in Eq. (24) create the ion of interest. These include direct ionization from the primary beam and charge exchange with buffer gas ions and molecular impurity ions. The coefficients a to c represent the reaction rates of the charge exchange processes, which are estimated to be of the order of $10^{-9} - 10^{-10}$ cm^3/s as discussed in Section 3. The ions can be lost via three-body recombination with a buffer gas atom and an electron (the rate defined by α of Eq. (2) if X is He), molecular formation with buffer gas impurities and ion guide evacuation, λ_{evac}. It is simple to add further reaction processes if necessary.

For an ion of interest, a molecule, a buffer gas atom or an electron, the simulation output provides an evolution of the number density (ions/cm^3) as a function of time in volume C of Fig. 12. The absolute number density does not represent the number of mass-separated ions/s detected on the channel plates downstream of the focal plane of the IGISOL mass separator, however it can be used to understand the competitive processes in the ion guide and the sensitivity to the various coefficients. One example of the output of the simulation is given in Fig. 13 which illustrates the sensitivity of the time profiles of Y^+, YO^+ and YO^+H_2O to the production rate of yttrium atoms from the filament.

For all three values of n simulated in Fig. 13, the time profile of Y^+ shows an initial peak. On the other hand, for the molecular species two peaks are seen. The creation of the first peak is strongly coupled to the evaporation rate of yttrium atoms from the filament and the initial saturation density in the beam region. In order to have the two peaks of YO^+ approximately the same amplitude (matching more closely the experimental time profile in Fig. 11) the production rate should be lower than the estimated value. The $YO^+(H_2O)$ time profile suggests a delayed second peak, following an initial decrease of the equilibrated number density.

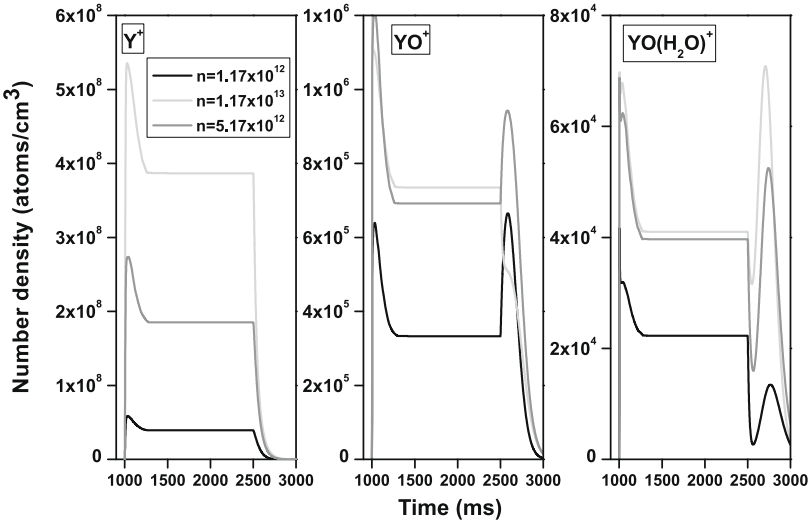

Fig. 13. Simulation time profiles of Y^+, YO^+ and $YO^+(H_2O)$ as a function of the initial production rate n from the filament. The primary beam is turned on at 1 s and off at 2.5 s.

Although the drop is not seen experimentally, the second peak is reproduced.

In a similar manner to the experimental observations, when the primary beam is turned off, the yttrium ion density decays whereas the molecular species show a pronounced increase prior to decay. This occurs in the simulation as a result of the competition between some of the different processes which are being modeled: charge exchange, three-body neutralization, two-body recombination, molecular formation and evacuation. Fig. 14 shows the sum evolution of all creative and destructive processes as a function of time following the turn off of the primary beam at 2.5 s to illustrate the difference between the profiles of Y^+ and $YO^+(H_2O)$. In the case of yttrium, there is no dominant positive process when the beam is turned off, the negative processes are the major contributor to the time profile and a peak is not created. On the other hand, a peak is created in $YO^+(H_2O)$ because the balance of the processes initially favours those of ion creation (ion survival). A maximum is reached when the balance between the "positive" and "negative" processes is momentarily equal, then the loss processes become the dominant factor and thus the count rate drops. All competing processes are in equilibrium when the count rate is saturated.

Similar studies have been performed on technetium and bismuth which, unlike yttrium, are very insensitive to molecular formation. Additionally, such studies have not only been performed in helium buffer gas but also in argon, and suggest that the chemical nature of the ion of interest and the buffer gas-type are important parameters in understanding the experimental data. A more detailed publication discussing the above competitive process model and related experiments will be submitted in the future.

In the second approach to explaining the origin of the beam-related spikes we have considered the effect of the electric field generated by the plasma as discussed in Section 4.2, in the case of a pulsed primary beam. Previously, we showed how the continuous primary beam can affect the transport efficiency and evacuation time of the ions through the evacuation channel of the LISOL laser ion guide. Fig. 15 illustrates the time structure of the ions created in the beam area (a volume of $\sim 3\ cm^3$ in the left hand side of the channel shown in Fig. 8) during a 1 s beam pulse followed by transportation through the channel. As the plasma density increases a well-pronounced peak occurs at the beginning of the time profile. In this instance, the count rate increases during the time in which the plasma has yet to fully develop in the channel. After ~100 ms the number of counts starts to reduce reflecting a fully developed plasma and a reduced transmission efficiency. The second peak corresponds to the evacuation of residual ions from the beam area after the suppression effect of the plasma has disappeared.

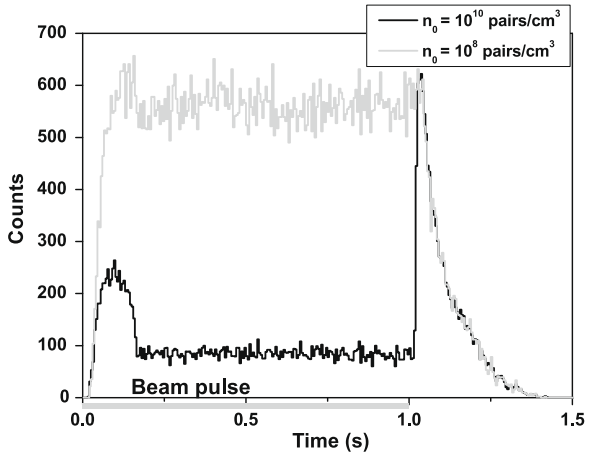

Fig. 15. Simulated time profiles of evacuated ions created in the beam area for an initial plasma density of $10^{10}\ cm^{-3}$ (black) and $10^8\ cm^{-3}$ (light grey). The recombination of the transported ions was not included in the simulation.

Quantitative comparisons with the experimental data have not been performed and this approach only serves to illustrate that the plasma-generated field can generate similar structures as seen in the experimental data. Other effects not discussed here include the role of diffusion of the plasma, realistic beam and gas flow distributions and the different mobility of the studied ions and plasma ions. It is encouraging however, that even in a relatively simple model we can recreate some of the features of the ion transport. We expect that similar features will be seen in other gas cell geometries involving an inhomogeneous ionization of the gas media by the primary beam. Time profiles containing beam-generated spikes have been observed using the HIGISOL ion guide and the light-ion ion guide. On the other hand, such fea-

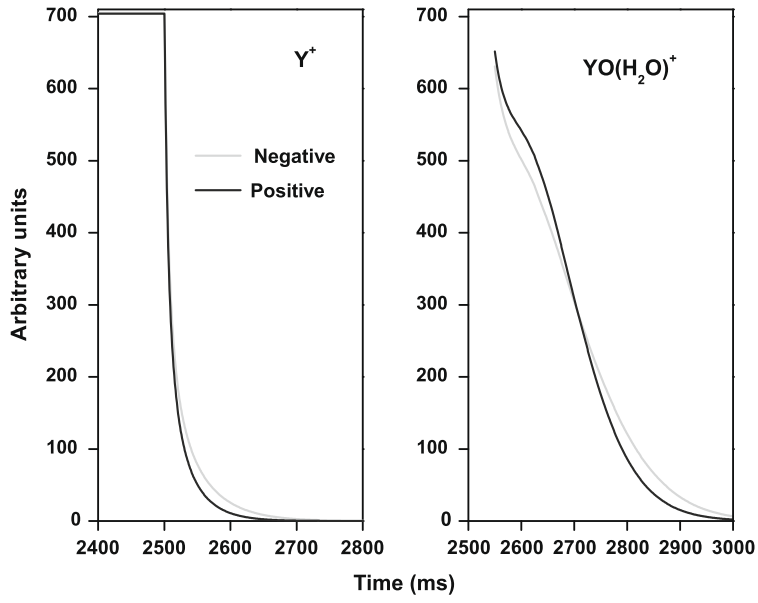

Fig. 14. The sum of the positive and negative processes following turn off of the primary beam at $t = 2.5$ s for Y^+ and $YO^+(H_2O)$ as a function of time.

tures have not been observed in the fission ion guide (albeit only $^{112}Rh^+$ and $^{129}Xe^+$ time profiles have been studied [46]) and if seen, would be more likely to be associated with competition processes between creative and destructive reactions, rather than to the ionization density which is homogeneous due to the isotropy of the fission fragment distribution.

Finally, we note that in rather different environments to that of the ion guide discussed here, the formation of so-called "after-peak" pulses are common occurrences observed in the afterglow of pulsed discharges. The role of Ar_2^+ ions and dissociative recombination has been identified as important mechanisms [47,48] giving rise to such effects. Similarly, electron cyclotron resonance (ECR) ion sources can be operated either in a continuous mode or in an afterglow mode. In the latter mode, when the microwave power heating the electrons on the resonance is switched off, the intensities of highly-charged ion beams increase [49]. This peculiar phenomenon can be exploited by pulsing the microwaves.

5. Evolution of a stopped primary beam of $^{89}Y^{21+}$

Several gas catchers have successfully stopped and extracted energetic beams, degraded in energy before entering the gas cell, in order to probe the stopping and extraction efficiency as a function of the incoming beam intensity [5–8]. In this section we discuss the stopping in the LISOL ion guide of a primary beam of $^{89}Y^{21+}$ of energy 623 MeV (~7 MeV/u), delivered from the Jyväskylä K-130 cyclotron. The dependence on the extracted yttrium yield as a function of the ionization-rate density has been previously discussed by Moore [9] in connection with the JYFL laser ion guide and will not be presented here. Rather, we highlight the count rate dependence of the stopped yttrium as a function of gas pressure and buffer gas-type, compared to the corresponding yield of YO^+ which is formed during the extraction of the stopped Y^+. The trend of the ratio of Y^+/YO^+ is discussed in a simple framework involving some of the competing processes presented in Section 4.3 – in this instance the stopped fraction of yttrium, the buffer gas purity, the different recombination coefficients and the different evacuation times due to the exit nozzle conductance.

A rotating nickel degrader foil of thickness 12.5 μm was installed ~80 mm upstream from a collimator of 6 mm in diameter attached to the side of the ion guide used to optimize the primary beam tuning. At 0° the energy of the primary beam is reduced to ~235 MeV. The thicknesses of the degrader and Havar window were accurately determined by measuring the energy loss of α particles emitted from a ^{241}Am source [39]. The result was cross-checked with a SRIM simulation [50]. Fig. 16 shows the results of the mass-separated ion yield when the degrader angle was tuned to 45°, a thickness of 17.7 μm, as a function of both helium and argon buffer gas pressure. The cyclotron beam intensity was 17 and 100 enA during the measurements with helium and argon, respectively. A clear maximum is observed when using argon at a pressure of ~385 mbar, whereas over the available pressure range of helium a peak is not observed.

Fig. 17 shows the ratio of Y^+/YO^+ as a function of the respective gas pressure. A strikingly different behaviour in the dependence of the ratio is observed at pressures below ~250 mbar following which a convergence to a value of ~1.5 is reached. The time evolution of Y^+ and YO^+ ions in the buffer gas is described in a simple manner as follows:

$$\frac{d[Y^+]}{dt} = N_{Y^+} - k[M]\cdot[Y^+] - \alpha n_e(t)\cdot[Y^+],$$
$$\frac{d[YO^+]}{dt} = k[M]\cdot[Y^+] - k[M']\cdot[YO^+] - \beta n_e(t)\cdot[YO^+]. \quad (25)$$

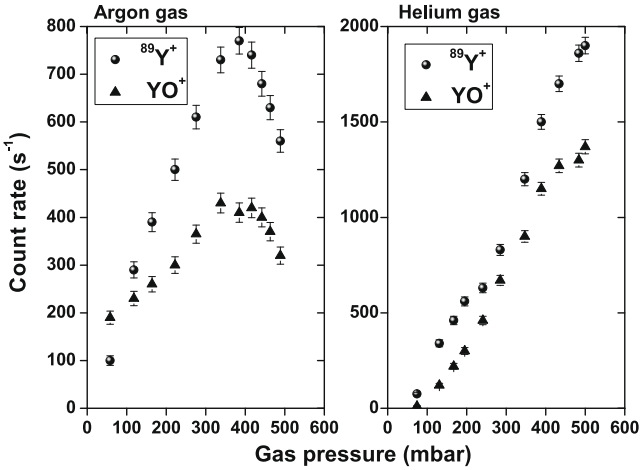

Fig. 16. Mass-separated yields of stopped $^{89}Y^+$ in both helium and argon buffer gases. The molecular formation of YO^+ is shown for comparison.

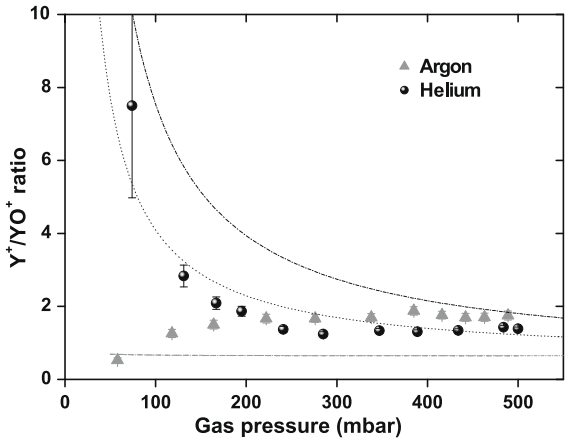

Fig. 17. The ratio Y^+/YO^+ as a function of pressure for helium and argon buffer gas. The dashed line represents the function obtained using Eq. (26) for Ar, the dot–dashed line for He and the dotted line following a reduction of a factor of 2 in the dissociative recombination coefficient β for YO^+ in He (see text for discussion).

In these two rate equations, N_Y^+ refers to the production rate of the Y^+ ionic state by, for example, laser ionization or stopped primary beam, k represents the molecular reaction rate constant [51] (it is correct to assume that the rate constant for Y^+ reacting with O_2 is within the same order of magnitude as that for YO^+ reacting with H_2O [1]), and the two-body dissociative recombination coefficient $\beta = 3\times10^{-6}\,cm^3\,s^{-1}$ [45]. The other parameters have been defined in Section 4.3. At time $t = 0$, yttrium ions are present within the beam region in an equilibrium balance and during evacuation the only processes modeled are neutralization and molecular formation. The model is very simple and does not take into account losses to the walls of the ion guide due to diffusion. However, for the ratio of Y^+/YO^+ neither the actual feeding rate nor eventual loss mechanisms are of importance as they effect both ionic species in a similar way.

Eq. (25) can be simplified because the characteristic time τ for the plasma to reach equilibrium (Eq. (11)) is far smaller than the evacuation time from the beam region, t_{evac}. Hence, the ion-electron density $n(t)$ of Eq. (20) can be written $\sim 1/\alpha t_{evac}$. Note that with this approximation, information on the plasma equilibrium density n_0 is no longer required. In the case of a steady-state equilibrium, Eq. (25) = 0 and can be solved for Y^+/YO^+,

$$\frac{Y^+}{YO^+} = \frac{k[M'] + \beta/\alpha t_{evac}}{k[M]} = \frac{k[M']}{k[M]} + \frac{\beta}{k[M]\alpha t_{evac}}. \quad (26)$$

The first term in the final expression describes the ratio of the molecular loss rates of Y^+ and YO^+ and is dominant at high pressures for both gases, where the effect of recombination can be neglected in comparison to molecular formation. The second term has an explicit pressure dependence due to the molecular reaction rate $k[M]$. This simple formula can be used to reproduce the general trend of the experimental ratios of Fig. 17. When using Ar buffer gas, both the recombination coefficient and the evacuation time are larger than for helium and the second term can be neglected, thus Eq. (26) becomes a constant. In helium, Eq. (26) describes a decrease of the Y^+/YO^+ ratio as a function of pressure.

The values for α and β are fixed, as is the evacuation time of the gas cell from the beam region in both helium and argon. The time scales for molecular formation in helium to a first approximation have been extracted from Table 4 of Ref [1]. The loss rate of yttrium to yttrium oxide is therefore defined by a molecular formation time of 9 ms while the loss of yttrium oxide in the reaction with water, 14 ms. In argon we simply assume an increase of a factor of 10 in the impurity level compared to helium according to the grade of the gas bottle. Fig. 17 additionally compares the result of the simulation to that of the experimental data, the simulation represented by dashed and dot–dashed lines for Ar and He, respectively. It is clear that although the simulated ratio does not fit the experimental data well, the general trend can be reproduced, showing a steady decline of the ratio in He gas and a constant level in Ar. Note that as the pressure $P \to \infty$, the simulated ratio converges to $\sim$0.65, independent of the buffer gas used. This simply reflects the ratio of the two molecular timescales given above. The strength of the slope of the fit in helium is defined by α and β. The value for β is suggested to be an upper limit for molecular recombination [45] and if reduced by a factor of 2 then a better agreement with the data is obtained (dotted line in Fig. 17).

We can provide an estimate of the impurity levels of oxygen and water by fitting to the ratio data in helium gas and following the assumptions made in Section 3.2 of Ref. [1]. The fit function follows the form of the final expression in Eq. (26), $Y^+/YO^+ = A + B/P$. The two constants A and B represent the first and second term (excluding the explicit pressure dependence) in Eq. (26), respectively. The errors on the experimental ratios in Fig. 17 have only been estimated from the square root of the count rates in Fig. 16. After scaling the errors according to the square root of the reduced chi-squared of the fit, the results for A and B are 1.09(2) and 107(53), respectively. The size of the error on B reflects the uncertainty of the fit at the lowest pressures. Nevertheless, using the obtained constants one can extract an estimate for the impurity levels of oxygen and water during the conditions of this experiment, $\sim$0.5 ppm for each contaminant, respectively. These numbers can be compared with those extracted from the March 2006 off-line data of Ref. [1], 73 and 101 ppb, respectively. At first glance it may seem that the conditions in the present work, undertaken several months after March 2006, are even more impure. However, if the value for β is smaller than assumed here then the extracted impurity levels also reduce (for the same fitting constants A and B). Additionally, the errors on the fitting have been ignored for the present discussion. By the second set of off-line experiments in March 2007 the impurity level had been improved to sub-ppb conditions. If the measurements described here were undertaken in such pure conditions then we may not have had the opportunity to study the processes described in this section.

Finally, we note that it is not our intention to extract detailed numbers from this simple model but to provide an explanation for the behaviour of the ratio of Y^+/YO^+ in different buffer gas environments. We have shown that using only a few parameters including the impurity concentration in the two buffer gases, the evacuation time from the gas cell and the recombination coefficients, the different trends in the data sets can be understood.

6. Conclusions and outlook

A series of experiments have been performed in order to gain a better understanding of the processes occurring within a gas cell under on-line conditions. This is particularly important for future work with an on-line laser ion source as the optimum conditions of the IGISOL technique are not the same as those required to access a neutral fraction with selective laser ionization. In a continuation to our earlier work on the studies of molecular formation processes with yttrium, a particularly chemically active ion, we have added additional complexity to this picture by introducing a primary beam into the gas cell. Studies of time profiles of yttrium and associated molecules have provided insight not only into the saturated yields but also the dynamic, competing effects involved when the primary beam is operated in a pulsed mode. During the evacuation of an ion from the gas cell a number of creative and destructive processes occur which determine the final state of the ion, whether neutral, ionic or in a molecular form. Often, surprising dynamic effects have been seen which are closely linked to the chemical nature of the element.

The introduction of resonant laser excitation and ionization has been discussed in terms of an *effective volume* for laser ionization, probed with and without the presence of a primary beam. Off-line, the volume defined by the presence of molecular impurities can be increased significantly by reducing the level of impurities within the gas cell [1]. However, the accessible neutral fraction in the presence of a primary beam has been shown to be restricted to the nozzle region, an effective volume only $\sim$0.7% of the total volume of the ion guide which is evacuated within ms. We have shown that recombination of the buffer gas alone cannot explain the survival of a neutral fraction close to the exit nozzle. A variety of processes in the gas cell have been discussed, including molecular formation, recombination, the role of impurities and charge exchange leading to ion creation, and the generation of a plasma field within the gas cell. All of these processes are competing for ion creation, ion survival and ion destruction. In order to understand why the neutral fraction accessible to laser ionization is restricted close to the nozzle it is possible to rule out several of the processes discussed in this article. The complexity of the plasma-generated electric field may indicate the suppression of ion transportation in the gas cell and thus could be suggested as a mechanism which restricts the effective volume. However, presently we do not have sufficient information to confirm such a mechanism.

It is clear that laser ionization needs to be applied in a zone where the ion-electron pair density is low enough for the laser-produced ions to survive. At the same time, under circumstances in which the laser ionization scheme is non-optimal resulting in a lower probability of re-ionizing in a single laser shot, it is important to increase the effective volume for re-ionization such that the atoms can be interrogated by multiple shots. In order to address these issues the laser ionization zone should not be visible to the accelerator beam path or to the trajectories of recoils or scattered particles. One such ion guide design has recently been developed by the LISOL group and consists of separated stopping and laser ionization chambers [52]. The first tests of this new concept have shown that recombination of laser-produced ions can be avoided. A similar gas cell has been constructed at the IGISOL facility, JYFL, and first tests will be reported in the future.

Acknowledgments

This work has been supported by the LASER Joint Research Activity project under the EU 6th Framework program "Integrating Infrastructure Initiative – Transnational Access", Contract No. 506065 (EURONS) and by the Academy of Finland under the Finnish centre of Excellence Program 2006–2011 (Nuclear and Accelerator Based Physics Program at JYFL). The support via the Finnish–Russian Interacademy Agreement (Project No. 8) is acknowledged.

References

[1] T. Kessler, I.D. Moore, Y. Kudryavtsev, K. Peräjärvi, A. Popov, P. Ronkanen, T. Sonoda, B. Tordoff, K. Wendt, J. Äystö, Nucl. Instrum. Meth. B 266 (2008) 681.
[2] P. Karvonen, I.D. Moore, T. Sonoda, T. Kessler, H. Penttilä, K. Peräjärvi, P. Ronkanen, J. Äystö, Nucl. Instrum. Meth. B 266 (2008) 4794.
[3] M. Huyse, M. Facina, Y. Kudryavtsev, P.V. Duppen, ISOLDE collaboration, Nucl. Instrum. Meth. B 187 (2002) 535.
[4] M. Facina, B. Bruyneel, S. Dean, J. Gentens, M. Huyse, Y. Kudryavtsev, P. Van den Bergh, P. Van Duppen, Nucl. Instrum. Meth. B 226 (2004) 401.
[5] L. Weissman, D. Morrissey, G. Bollen, D. Davies, E. Kwan, P. Lofy, P. Schury, S. Schwarz, C. Sumithrarachchi, T. Sun, R. Ringle, Nucl. Instrum. Meth. A 540 (2005) 245.
[6] A. Takamine, M. Wada, Y. Ishida, T. Nakamura, K. Okada, Y. Yamazaki, T. Kambara, Y. Kanai, T.M. Kojima, Y. Nakai, N. Oshima, A. Yoshida, T. Kubo, S. Ohtani, K. Noda, I. Katayama, P. Hostain, V. Varentsov, H. Wollnik, Rev. Sci. Instrum. 76 (2005) 103503.
[7] J. Neumayr, L. Beck, D. Habs, S. Heinz, J. Szerypo, P. Thirolf, V. Varentsov, F. Voit, D. Ackermann, D. Beck, M. Block, Z. Di, S. Eliseev, H. Geissel, F. Herfurth, F. He[ss]berger, S. Hofmann, H.-J. Kluge, M. Mukherjee, G. Munzenberg, M. Petrick, W. Quint, S. Rahaman, C. Rauth, D. Rodriguez, C. Scheidenberger, G. Sikler, Z. Wang, C. Weber, W. Pla[ss], M. Breitenfeldt, A. Chaudhuri, G. Marx, L. Schweikhard, A. Dodonov, Y. Novikov, M. Suhonen, Nucl. Instrum. Meth. B 244 (2006) 489.
[8] G. Savard, J. Clark, C. Boudreau, F. Buchinger, J.E. Crawford, H. Geissel, J.P. Greene, S. Gulick, A. Heinz, J.K.P. Lee, A. Levand, M. Maier, G. Münzenberg, C. Scheidenberger, D. Seweryniak, K.S. Sharma, G. Sprouse, J. Vaz, J.C. Wang, B.J. Zabransky, Z. Zhou, Nucl. Instrum. Meth. B 204 (2003) 582.
[9] I.D. Moore, Nucl. Instrum. Meth. B 266 (2008) 4434.
[10] K. Peräjärvi, J. Cerny, J. Hakala, J. Huikari, A. Jokinen, P. Karvonen, J. Kurpeta, D. Lee, I. Moore, H. Penttilä, A. Popov, J. Äystö, Nucl. Instrum. Meth. A 546 (2005) 418.
[11] B. Tordoff, T. Eronen, V. Elomaa, S. Gulick, U. Hager, P. Karvonen, T. Kessler, J. Lee, I. Moore, A. Popov, S. Rahaman, S. Rinta-Antila, T. Sonoda, J. Äystö, Nucl. Instrum. Meth. B 252 (2006) 347.
[12] J. Ärje, J. Äystö, H. Hyvönen, P. Taskinen, V. Koponen, H. Honkanen, A. Hautojärvi, K. Vierinen, Phys. Rev. Lett. 54 (1985) 99.
[13] R. Béraud, A. Emsallem, A. Astier, R. Bouvier, R. Duffait, Y. Le Coz, S. Morier, A. Wojtasiewicz, Y.A. Lazarev, I.V. Shirokovsky, I.N. Izosimov, D. Barneoud, J. Genevey, A. Gizon, R. Guglielmini, G. Margotton, J.L. Vieux-Rochaz, Nucl. Instrum. Meth. A 346 (1994) 196.
[14] P. Dendooven, R. Béraud, E. Chabanat, A. Emsallem, A. Honkanen, M. Huhta, A. Jokinen, G. Lhersonneau, M. Oinonen, H. Penttilä, K. Peräjärvi, J.C. Wang, J. Äystö, Nucl. Instrum. Meth. A 408 (1998) 530.
[15] M. Oinonen, R. Béraud, G. Canchel, E. Chabanat, P. Dendooven, A. Emsallem, S. Hankonen, A. Honkanen, J. Huikari, A. Jokinen, G. Lhersonneau, C. Miehé, A. Nieminen, Y. Novikov, H. Penttilä, K. Peräjärvi, A. Popov, D.M. Seliverstov, J.C. Wang, J. Äystö, Nucl. Instrum. Meth. A 416 (1998) 485.
[16] R.J. van Sonsbeek, R. Cooper, R.N. Bhave, J. Chem. Phys. 97 (1992) 1800.
[17] R. Cooper, R.J. van Sonsbeek, R.N. Bhave, J. Chem. Phys. 98 (1993) 383.
[18] D. Bates, S. Khare, Proc. Phys. Soc. 85 (1965) 231.
[19] T. Martens, A. Bogaerts, W.J.M. Brok, J.V. Dijk, Appl. Phys. Lett. 92 (2008) 041504.
[20] D. Morrissey, G. Bollen, M. Facina, S. Schwarz, Nucl. Instrum. Meth. B 266 (2008) 4822.
[21] E. McDaniel, Collision Phenomena in Ionized Gases, John Wiley and Sons, New York, 1964.
[22] A.R. Turner-Smith, J.M. Green, C.E. Webb, J. Phys. B 6 (1973) 114.
[23] J.M. Green, C.E. Webb, J. Phys. B 7 (1974) 1698.
[24] P.G. Browne, M.H. Dunn, J. Phys. B 6 (1973) 1103.
[25] R. Deloche, P. Monchicourt, M. Cheret, F. Lambert, Phys. Rev. A 13 (1976) 1140.
[26] R. Johnsen, M.T. Leu, M.A. Biondi, Phys. Rev. A 8 (1973) 1808.
[27] E. Graham, M.A. Biondi, R. Johnsen, Phys. Rev. A 13 (1976) 965.
[28] C.P. de Vries, H.J. Oskam, Phys. Rev. A 19 (1979) 2095.
[29] R. Johnsen, M.A. Biondi, J. Chem. Phys. 73 (1980) 5045.
[30] D.W. Ernie, H.J. Oskam, Phys. Rev. A 23 (1981) 325.
[31] P. Baltayan, J.C. Pebay-Peyroula, N. Sadeghi, J. Phys. B 18 (1985) 3615.
[32] P. Baltayan, J.C. Pebay-Peyroula, N. Sadeghi, J. Phys. B 19 (1986) 2695.
[33] R.R. Arslanbekov, R.C. Tobin, A.A. Kudryavtsev, J. Appl. Phys. 81 (1997) 554.
[34] A. Bogaerts, R. Gijbels, J. Appl. Phys. 92 (2002) 6408.
[35] K. Tachibana, Phys. Rev. A 34 (1986) 1007.
[36] J.H. Kolts, D.W. Setser, J. Chem. Phys. 68 (1978) 4848.
[37] J. Hakala, V.-V. Elomaa, T. Eronen, U. Hager, A. Jokinen, J. Äystö, Nucl. Instrum. Meth. B 266 (2008) 4628.
[38] COMSOL AB, COMSOL Multiphysics, third ed., Stockholm, Sweden, 2007.
[39] T. Kessler, Development and Application of Laser Technologies at Radioactive Ion Beam Facilities, Ph.D. Thesis, University of Jyväskylä, 2008.
[40] K. Peräjärvi, P. Dendooven, J. Huikari, A. Jokinen, V.S. Kolhinen, A. Nieminen, J. Äystö, Nucl. Instrum. Meth. A 449 (2000) 427.
[41] K. Peräjärvi, Studies of Ion Transport in Gases – Applications in Nuclear Physics, Ph.D. Thesis, University of Jyväskylä, Jyväskylä, 2001.
[42] I. Wolfram, Research, sixth ed., Mathematica, Champaign, Illinois, 2007.
[43] G.M. Petrov, S. Atanassova, D. Zhechev, G.V. Mishinsky, V.I. Zhemenik, J. Plasma Phys. 68 (2002) 321.
[44] M. Facina, A Gas Catcher for the Selective Production of Radioactive Beam Through Laser Ionization, Ph.D. Thesis, IKS Leuven, 2004.
[45] Y. Kudryavtsev, B. Bruyneel, M. Huyse, J. Gentens, P. Van den Bergh, P. Van Duppen, L. Vermeeren, Nucl. Instrum. Meth. B 179 (2001) 412.
[46] P. Dendooven, private communication.
[47] A. Bogaerts, R. Gijbels, G.P. Jackson, J. Anal. Atom. Spectrom. 18 (2003) 533.
[48] A. Bogaerts, J. Anal. Atom. Spectrom. 22 (2007) 502.
[49] R. Geller, Electron Cyclotron Resonance Ion Sources and ECR Plasmas, Institute of Physics Publishing, 1996.
[50] J. Ziegler, J. Biersack, Srim, <http://www.srim.org>, 2006.
[51] G.K. Koyanagi, D. Caraiman, V. Blagojevic, D.K. Bohme, J. Phys. Chem. A 106 (2002) 4581.
[52] Yu. Kudryavtsev, T.E. Cocolios, J. Gentens, M. Huyse, O. Ivanov, D. Pauwels, T. Sonoda, P. Van den Bergh, P. Van Duppen, Nucl. Instrum. Meth. B 267 (2009) 2908.